Delaying Effect of Cementite on Recrystallization Kinetics of a Ti-Nb Microalloyed High-Formability Steel

ARTHUR MARCEAUX DIT CLÉMENT, KHALID HOUMMADA, JOSÉE DRILLET, VÉRONIQUE HÉBERT, and PHILIPPE MAUGIS

Annealing of cold-rolled high-strength steels leads to various microstructural changes such as recrystallization, cementite precipitation, microalloying elements precipitation and austenite formation. These transformations are expected to interact with each other. Understanding how and where austenite forms in a microstructure is of prime importance to avoid formation of banded microstructures, which are detrimental to good in-use properties. In this work, a mean-field model is used to simulate concomitant recrystallization, cementite precipitation, microalloying elements precipitation and austenite formation kinetics, as well as their interactions during 1 and 10 °C/s heating. Excellent agreement with experimental data is obtained only if cementite pinning effect on recrystallized grain boundaries is considered. It is shown that cementite exhibits a much stronger delaying effect on recrystallization kinetics than microalloying elements, leading to the formation of banded microstructures. Carbon nominal content of a steel appears to be the most important parameter to acknowledge to understand recrystallization kinetics.

I. INTRODUCTION

HIGH-STRENGTH steels (HSS) are widely used in the automotive industry to help manufacturers reach their goals of greenhouse gases emissions reduction without compromising passenger safety.[1–3] High-formability steels are a subtype of HSS for which nominal carbon content is increased (compared to low-carbon dual-phase steels) to stabilize austenite (γ) crystals at room temperature and benefit from TRIP effects, giving the steel higher tensile elongation.

Manufacturing high-formability steels involves a cold-rolling step before intercritical annealing, during which a certain volume fraction of austenite is formed. Upon cooling, austenite decomposes into several products and gives the steel its final microstructure, from which the mechanical properties (yield strength, tensile elongation, …) and in-use properties (formability, weldability, hole expansion ratio) result. Homogeneous distribution of phases in the final microstructure is of prime importance, as so-called *banded* microstructures are detrimental to good formability properties. It is, therefore, essential to understand how and where austenite forms in the microstructure during annealing.

Austenite formation has already been studied for many combinations of chemistries, microstructures and steel conditions (hot- or cold-rolled).[4–24] Indeed, each transformation kinetics will depend on the steel nominal chemistry, initial microstructure, manufacturing process and subsequent annealing parameters. The possible overlap of transformations offers many interaction possibilities, leading to numerous scenarii of microstructural evolutions from one steel to another. Understanding how transformations interact with each other is thus essential for who wants to accurately predict if a given annealing process will lead to the formation of a banded microstructure.

To this end, many authors have taken interest in the study of how incomplete recrystallization affects austenite formation scenario and kinetics.[6,7,10,12–14,16,19,23,24] The influence of microalloying elements such as Ti or Nb on recrystallization kinetics (in ferrite or austenite) has also been a topic of interest for a long time, and led to modelling efforts regarding their precipitation kinetics.[24–33] However, it is surprising to notice that

ARTHUR MARCEAUX DIT CLÉMENT is with the CNRS, IM2NP, Aix Marseille Univ, Campus de Saint Jérôme - Case 142, Avenue Escadrille Normandie Niemen, 13397 MARSEILLE Cedex 20, France. and also with the ArcelorMittal Maizières Research SA, Voie Romaine, 57280 Maizières les Metz, France. Contact e-mail: arthur.marceauxditclement@live.fr KHALID HOUMMADA and PHILIPPE MAUGIS are with the CNRS, IM2NP, Aix Marseille Univ. JOSÉE DRILLET and VÉRONIQUE HÉBERT are with the ArcelorMittal Maizières Research SA.

cementite precipitation has only scarcely been considered in the available literature.[34–36] Moreover, these works do not take interest in how it might affect recrystallization kinetics.

This lack of studies about cementite precipitation and recrystallization kinetics could be linked to most of the available literature being dedicated to low-carbon chemistries (≤ 0.1 wt pct C)[6,10,13,14,17,18,20,24] or ferrite-pearlite initial microstructures, in which cementite precipitation does not occur.[6,7,12–14,16,17,19,23] Mainly, available studies focus on austenite formation mechanisms and not on *why* recrystallization can be incomplete.

The aim of this work is to investigate microstructural evolutions in a cold-rolled, high-carbon (0.2 wt pct) high-formability steel undergoing continuous heating (1 and 10 °C/s), and understand if cementite precipitation can affect recrystallization and other transformations through interactions between them, eventually leading to the formation of banded microstructures. A mean-field model for microstructural evolutions is developed to compare simulated kinetics to experimental data.

II. MATERIALS AND METHODS

The steel grade studied in this work was elaborated at ArcelorMittal Research Center in Maizières-lès-Metz, France. Its nominal composition is given in Table I. Initial microstructure after hot rolling and coiling at 545 °C was made of 65 vol pct bainite (α_B) and 35 vol pct martensite (α'). Cold rolling with 50 pct reduction was then applied (Figure 1). Samples for FEG-SEM observations were heat-treated at 1 °C/s (slow heating) or 10 °C/s (fast heating) on a DT1000 dilatometer, with interruption at desired temperatures by helium blowing. Conventional metallographic polishing was applied to these samples before DINO etching (140 mL distilled water, 100 mL H_2O_2, 4 g oxalic acid, 2 mL H_2SO_4, 1.5 mL HF). Micrographs were obtained on a FEG-SEM JEOL® JSM-7800F at quarter steel sheet thickness and phase fractions determined by random point counting method with Fiji software.[37] Samples for TEM observations and gravimetric analyses of electrolytic extraction residues were heat treated in an annealing simulator furnace with water quenching. TEM observations were performed on electro-thinned foils with a JEOL® JEM-2100F instrument at 200 kV. Modelling work was written in Python 2.7.16 language with Spyder 3.3.3 suite.

III. MICROSTRUCTURAL EVOLUTIONS DURING HEATING

A. *Microstructural Changes*

SEM micrographs of samples heated up to 670 °C, 690 °C, 710 °C and 730 °C at 1 and 10 °C/s heating rates are presented in Figures 2 and 3, respectively. DINO etching is used to reveal recrystallization.

Non-recrystallized zones show irregular surfaces while recrystallized grains appear polygonal with a smooth surface. Austenite is deeply etched and appears as darker valleys on grain boundaries. Relative carbide surface density helps to differentiate former martensite islands (high density) from former bainite (low density). Recrystallized grains will be referred to as recrystallized ferrite (α_{REX}), regardless of their mother phase.

During slow heating, recrystallization seems to start around 670 °C on α_B/α' interfaces but also in former martensite islands, where cementite mostly lies. Prior grain boundaries and carbides are indeed known to be nucleation sites for recrystallization.[38] At 690 °C, recrystallization has advanced. Big α_{REX} grains are seen in former martensite but also in what seems to be former bainite. Large parts of the microstructure are still deformed. At 710 °C, most of the microstructure is recrystallized. However, big α_{REX} grains are mostly found in former bainite, while the remaining non-recrystallized zones lie in former martensite. It also looks like α_{REX} grains are slightly smaller in former martensite. First austenite nuclei are seen on triple α_{REX} grain boundaries. At 730 °C, necklace austenite formation begins in former bainite and former martensite. Austenite nuclei are more numerous in former martensite. This could be due to the smaller grain size but also to a higher carbide density than in former bainite. The austenite nuclei density being different between former bainite and former martensite, a banded microstructure forms at higher temperature by preferential growth in former martensite, even though global recrystallization is close to 100 pct.

During fast heating, recrystallization starts around 710 °C on α_B/α' interfaces and in former martensite islands, similarly to what is observed with slow heating. At 730 °C, first austenite nuclei appear in a mostly non-recrystallized microstructure. They seem to be preferentially located in former martensite, where cementite almost exclusively lies. Some recrystallized grains are seen in cementite-depleted zones. Recrystallization thus seems to be favored in former bainite. At 750 °C, most austenite nuclei are found in former martensite. A few big α_{REX} grains are seen in former bainite. No recrystallization is seen in former martensite yet. At 790 °C, all former martensite has been turned into austenite (which transforms back into fresh martensite upon quenching). Non-recrystallized zones have been preferentially transformed into austenite. Microstructure thus mainly consists of alternating layers of fresh martensite (austenite) and big, elongated α_{REX} grains. A banded microstructure is obtained.

The studied steel exhibits an unusual recrystallization behavior. Previous studies led on low-carbon steels with bainite-martensite initial microstructures[18,24] showed that martensite recrystallized before bainite, allowing for the formation of homogeneous microstructures. However, it is observed here that if recrystallization does start in martensite, it is then fully achieved in bainite but not in martensite. A mean-field model for

Table I. Nominal Chemical Composition of Studied Steel

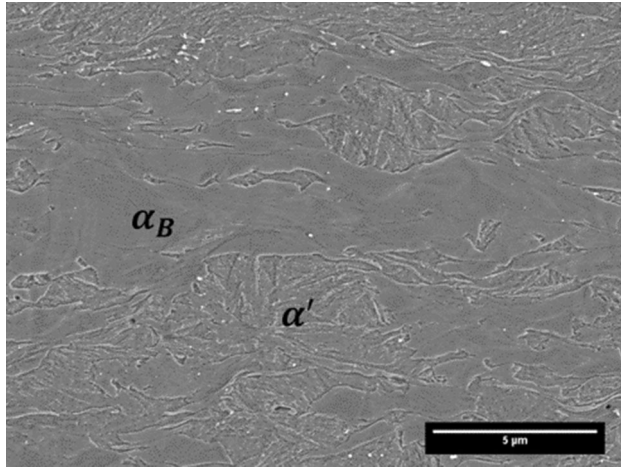|	C	Mn	Cr + Si	Nb	Ti	+ Al, N, B
[Weight Percent]	0.197	2.57	1.2	0.031	0.028	

Fig. 1—FEG-SEM micrograph of the initial cold-rolled microstructure of the studied steel. α_B stands for bainite (65 vol pct), α' for martensite (35 vol pct)—DINO etching.

microstructural evolutions is developed to understand why recrystallization happens that way.

B. Modelling

1. Model description

a. Austenite formation Austenite formation kinetics is modeled with JMAK theory.[39–43] Assuming site saturation for this transformation, the extended volume fraction is given by:

$$f_\gamma^e(t) = \frac{4}{3}\pi N_\gamma \left(\int_0^t dR_\gamma^e \right)^3 \qquad [1]$$

and true volume fraction comes from the JMAK equation:

$$f_\gamma(t) = 1 - \exp\left(-f_\gamma^e(t)\right) \qquad [2]$$

Growth rate of austenite grains in bainite and martensite is calculated through the evolution of the extended mean radius, which is the product of the austenitic transformation interface mobility and the transformation driving force:

$$M_\gamma(t) = M_\gamma^0 \exp\left(-\frac{Q_\gamma}{RT}\right) \qquad [3]$$

$$G_\gamma(t) = G_\gamma^0 \left(f_\gamma^{eq}(t) - f_\gamma(t)\right) \qquad [4]$$

Equilibrium volume fraction $f_\gamma^{eq}(t)$ is calculated with Thermo-Calc software with TCFE9 database.[44,45] All parameters are given in Table II.

b. Recrystallization Just like austenite formation, recrystallization kinetics are modeled with JMAK theory with site saturation assumption. As recrystallized grains can only grow in the non-recrystallized parts of the microstructure, following equations are obtained:

$$f_{REX}^e(t) = \frac{4}{3}\pi N_{REX} \left(\int_0^t dR_{REX}^e \right)^3 \qquad [5]$$

$$f_{REX}(t) = \exp\left(-f_\gamma^e(t)\right)\left(1 - \exp(-f_{REX}^e(t))\right) \qquad [6]$$

The evolution of the extended mean radius is described as the product of recrystallized grain boundaries mobility $M_{REX}^0(t)$ and recrystallization driving force $G_{REX}^0(t)$. They are however expected to be altered by microalloying elements precipitation (see Section III–B–2.).

$$M_{REX}^0(t) = \frac{D_{REX}^0}{RT}\frac{V_m^\alpha}{\lambda_{REX}}\exp\left(-\frac{Q_{REX}}{RT}\right) \qquad [7]$$

$$G_{REX}^0(t) = \frac{1}{2}\mu b^2 \rho \qquad [8]$$

All parameter values are indicated in Table III. Note that N_{REX}^{0,α_B} and $N_{REX}^{0,\alpha'}$ are fitted to ensure agreement with mean recrystallized grain radius (not shown in this paper).

c. Microalloying elements precipitation Nucleation stage

The microalloying elements precipitation model used in this study is based on the Deschamps-Bréchet model,[26,27] which involves calculation of two different stages for precipitation. First stage consists of nucleation and growth of precipitates, second of growth and coarsening of existing precipitates. Homogeneous nucleation of (Ti, Nb)C is assumed. Ti and Nb atoms are not differentiated. Ti/Nb atoms are thus represented by a mean microalloying element, whose properties are weighted between those of pure Ti and Nb, according to Ti and Nb relative quantities in the initially available solid solution (90 at. ppm Nb, 60 at. ppm Ti). All parameter values are indicated in Table IV.

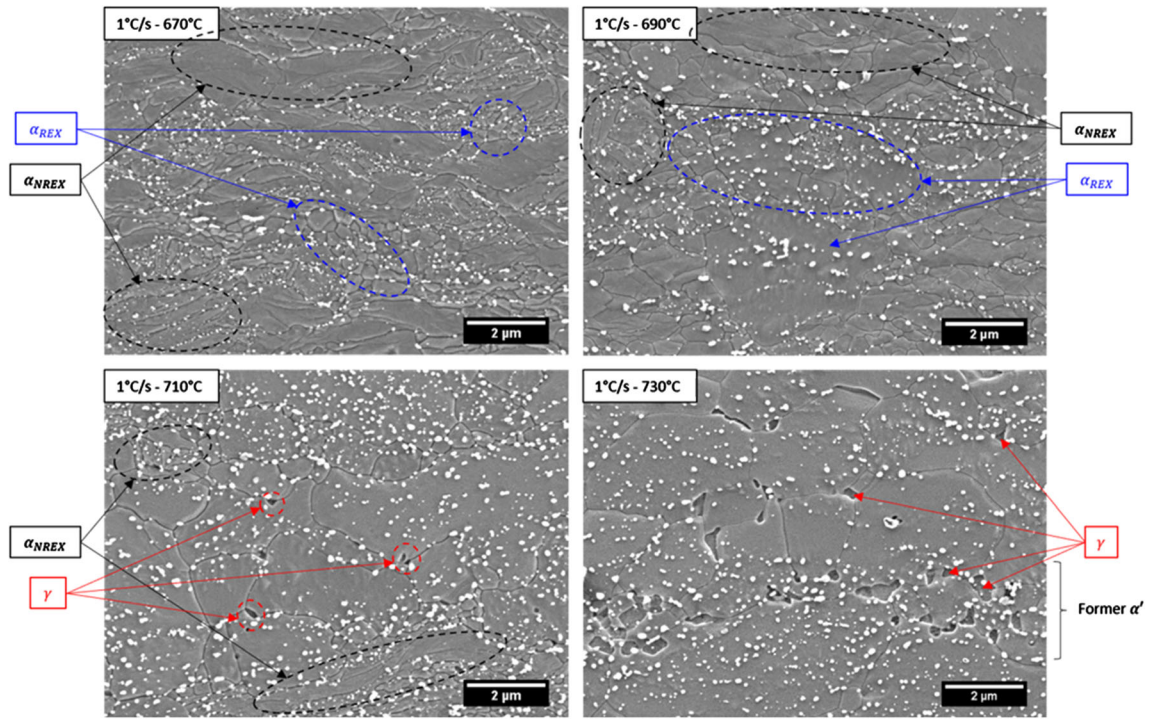The nucleation barrier and nuclei critical radius are:

Fig. 2—Microstructural changes during 1 °C/s heating. Former martensite and bainite can be distinguished by relative carbide density (higher in former martensite)—DINO etching.
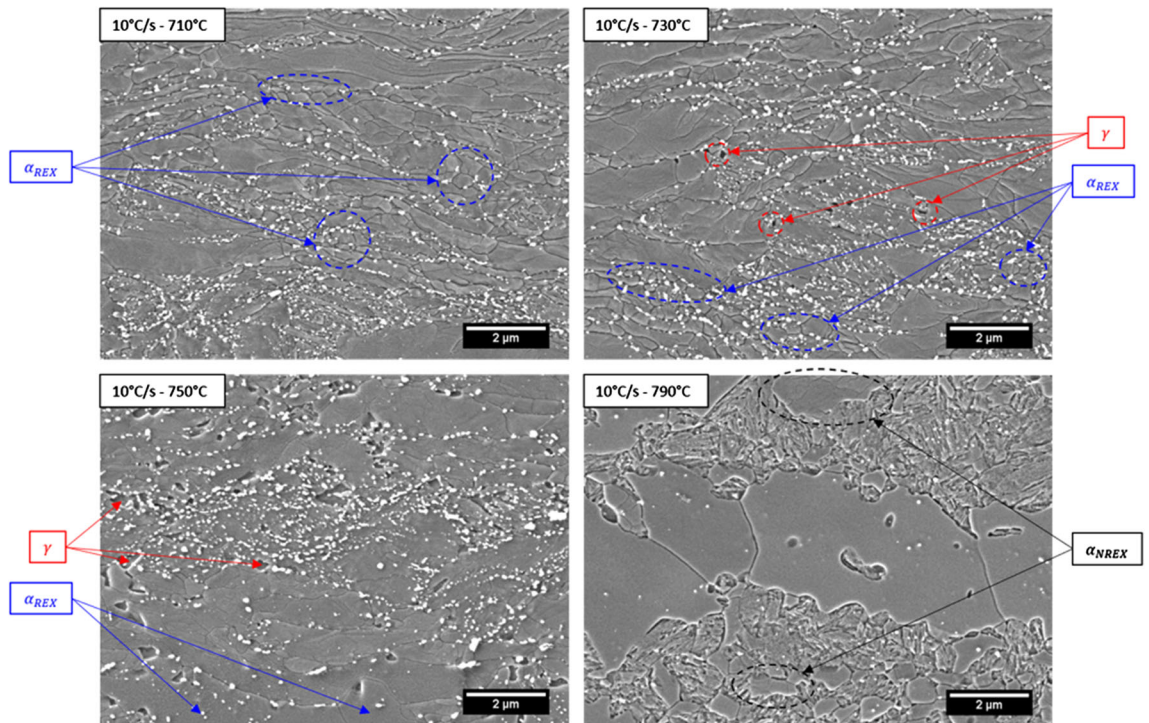

Fig. 3—Microstructural changes during 10 °C/s heating—DINO etching.

Table II. Parameters Used for the Austenite Formation Model

	Parameter	Value	Units	Literature Values
N_γ^{0,α_B}	Nucleation sites density for austenite formation in former bainite	8×10^{15}	m^{-3}	2×10^{16}[46]
$N_\gamma^{0,\alpha'}$	Nucleation sites density for austenite formation in former martensite	8×10^{16}	m^{-3}	
M_γ^0	Mobility of $\alpha \to \gamma$ transformation interface	0.0023	mol m J^{-1} s^{-1}	0.002 to 1[46–48]
Q_γ	Activation energy for austenite formation	140,000	J mol^{-1}	140,000[46–51]
G_γ^0	Prefactor for austenite formation driving force	100	J mol^{-1}	> 100[52]

Table III. Parameters Used for the Recrystallization Model

	Parameter	Value	Units	Literature Values
N_{REX}^{0,α_B}	Nucleation sites density for recrystallization in bainite	1×10^{16}	m^{-3}	5×10^{14} to 1×10^{16}[13,31]
$N_{REX}^{0,\alpha'}$	Nucleation sites density for recrystallization in martensie	5×10^{16}	m^{-3}	
$\rho_0^{\alpha_B}$	Dislocation density in bainite	8×10^{14}	m^{-2}	10^{13} to 10^{16}[53]
$\rho_0^{\alpha'}$	Dislocation density in martensite	1×10^{15}	m^{-2}	1×10^{15} [24]
D_{REX}^0	Prefactor for recrystallized grain boundary mobility	0.01	m^{2}s^{-1}	1.5×10^{-4}[31] 0.01 [24]
Q_{REX}	Activation energy for recrystallized grain boundary mobility	222000	J mol^{-1}	180000 to 290000[6,24,46,49]
γ_{GB}	Interfacial energy of recrystallized grain boundary	1.	J m^{-2}	0.56 to 1[24,31,49,54]
λ_{REX}	Grain boundary thickness	0.25×10^{-9}	m	
V_m^α	Ferrite molar volume	7.11×10^{-6}	m^{3}mol^{-1}	
μ	Ferrite shear modulus	80×10^9	Pa	
b	Dislocations Burgers vector in ferrite	2.5×10^{-10}	m	

$$\Delta G^* = \frac{16}{3}\pi\frac{\gamma_P^3}{\Delta g_v^2} \text{ and } R^* = -\frac{2\gamma_P}{\Delta g_v} \quad [9]$$

with γ_P the precipitate interfacial energy and Δg_v the nucleation driving force (per unit volume). For a regular solid solution, this driving force is[55]:

$$\Delta g_v = -\frac{RT}{V_m^P}\left(\ln\frac{x_{Ti,Nb}^{ss}}{x_{Ti,Nb}^{eq}} + \ln\frac{x_C^{ss}}{x_C^{eq}}\right) \quad [10]$$

It is assumed that C is at equilibrium between ferrite and cementite when (Ti,Nb)C precipitation occurs. The solubility limit of Ti/Nb in ferrite $x_{Ti,Nb}^{eq}$ is obtained through the solubility product of (Ti,Nb)C in ferrite (A and B being two constants):

$$\log\left(\left[x_{Ti,Nb}^{eq}\right]_{wt}\left[x_C^{eq}\right]_{wt}\right) = -\frac{A}{T} + B \quad [11]$$

Not all nuclei that reach the critical size will grow further. Some might dissolve back into the surrounding matrix. Only nuclei with a slightly higher radius than R^* will grow. Maugis and Gouné give the following corrected critical radius[56]:

$$R_{corr}^* = R^* + \frac{1}{2}\sqrt{\frac{k_B T}{\pi\gamma_P}} \quad [12]$$

The nucleation barrier value is very dependent on the interface energy value, whose experimental determination is challenging.[55,57] Thus, γ_P is often considered as an adjustable parameter of precipitation models. Therefore, it must be looked upon as an *effective* interfacial energy, which reflects several phenomena that might influence the precipitation kinetics, such as nucleation on lattice defects, non-sphericity of particles, anisotropy of true interfacial energy, stabilizing effects of alloying elements, *etc.* In our study, best fit between calculated and experimental kinetics is obtained with a value of γ_P = 0.72 J m^{-2}. It is close to the one found by Perez *et al.*[58] for Nb(C,N) precipitation in ferrite (0.78 J m^{-2}) with a similar model. Gouné *et al.* and Jang *et al.*[59,60] used values of 0.55 and 0.493 J m^{-2} for TiC precipitation in ferrite. Monte Carlo simulations by Gendt[61] led to a value of 1.22 J m^{-2} for NbC precipitation in ferrite.

Nucleation rate is given by:

$$\frac{dN}{dt}\bigg|_{nucl} = N_{(Ti,Nb)C}^0 Z\beta^* \exp\left(-\frac{\Delta G^*}{k_B T}\right)\left(1 - \exp\left(-\frac{t}{\tau}\right)\right) \quad [13]$$

where Z is Zeldovich parameter (probability of growth of a critical nucleus), β^* the absorption frequency of Ti/Nb atoms by a critical nucleus, and τ the incubation time.

$$Z = \frac{V_{at}^P}{2\pi R^{*2}}\sqrt{\frac{\gamma_P}{k_B T}}; \quad \beta^* = \frac{4\pi R^{*2} D_{Ti,Nb} x_{Ti,Nb}^{ss}}{a_\alpha^4};$$
$$\tau = \frac{4}{\pi}\frac{1}{2\beta^* Z^2} \tag{14}$$

Mean radius evolution due to nucleation of new precipitates is:

$$\left.\frac{dR}{dt}\right|_{nucl} = \frac{1}{N}\frac{dN}{dt}\left(R_{corr}^*(t) - R(t)\right) \tag{15}$$

Growth stage
Diffusion-controlled growth of existing precipitates is given by Zener's law:

$$\left.\frac{dR}{dt}\right|_{gr} = \frac{V_m^{Ti,Nb}}{V_m^\alpha}\frac{D_{Ti,Nb}}{R(t)}\left(x_{Ti,Nb}^{ss}(t) - x_{Ti,Nb}^i(t)\right) \tag{16}$$

Here, $x_{Ti,Nb}^i(t)$ is the Gibbs-Thomson-corrected Ti/Nb solubility at immediate vicinity of a spherical precipitate with $R(t)$ radius (R_0 is the capillarity radius, with $R_0 = \frac{2\gamma_P V_m^P}{R_{gp} T}$):

$$x_{Ti,Nb}^i(t) = x_{Ti,Nb}^{ss,eq}\exp\left(\frac{R_0}{R(t)}\right) \tag{17}$$

At each time step, one can now find the precipitate volume fraction:

$$f_v^{(Ti,Nb)C}(t) = N(t)\cdot\frac{4}{3}\pi R(t)^3 \tag{18}$$

and mass balance is ensured with:

$$x_{Ti,Nb}^{ss}(t) = x_{Ti,Nb}^0 - f_v^{(Ti,Nb)C}(t)\frac{V_m^\alpha}{V_m^P} \tag{19}$$

Coarsening stage
Diffusion-controlled coarsening of existing precipitates is given by:

$$\left.\frac{dR}{dt}\right|_{coar} = \frac{4}{27}\frac{V_m^P}{V_m^\alpha}\frac{D_{Ti,Nb}x_{Ti,Nb}^i(t)R_0}{R(t)^2} \tag{20}$$

During coarsening stage, equilibrium volume fraction of (Ti,Nb)C precipitates $f_{v,eq}^{(Ti,Nb)C}$ has been reached. It only changes with temperature (through the solubility product evolution) and can be found with a mass balance, accounting for Gibbs-Thomson effect:

$$f_{v,eq}^{(Ti,Nb)C}(t) = \left(x_{Ti,Nb}^0 - x_{Ti,Nb}^i(t)\right)\frac{V_m^P}{V_m^\alpha} \tag{21}$$

Precipitate density then diminishes when mean radius increases:

$$N_{coar}(t) = f_{v,eq}^{(Ti,Nb)C}(t)\cdot\left(\frac{4}{3}\pi R(t)^3\right)^{-1} \tag{22}$$

Transition from nucleation-growth to growth-coarsening stage
Mean radius evolution of all precipitates is calculated by considering the existence of two substages for precipitation, the first being the nucleation of new precipitates and their growth, the second being the growth and coarsening of existing precipitates. When more precipitates disappear by coarsening than new ones nucleate, substage transition is achieved. The criterion is:

$$-\left.\frac{dN}{dt}\right|_{coar} > \left.\frac{dN}{dt}\right|_{nucl} \tag{23}$$

Smooth transition from growth-controlled to coarsening-controlled mean radius evolution is done by using a coarsening transition function f_{tr}, so that in the first substage:

$$\frac{dN}{dt} = \left.\frac{dN}{dt}\right|_{nucl} \quad\text{and}\quad \frac{dR}{dt} = \left.\frac{dR}{dt}\right|_{nucl} + \left.\frac{dR}{dt}\right|_{gr} \tag{24}$$

while mean radius and precipitate density evolutions in the second substage are:

$$\frac{dN}{dt} = f_{tr}\left.\frac{dN}{dt}\right|_{coar} \quad\text{and}\quad \frac{dR}{dt} = (1-f_{tr})\left.\frac{dR}{dt}\right|_{gr} + f_{tr}\left.\frac{dR}{dt}\right|_{coar} \tag{25}$$

Perrard *et al.*[62] use the following function:

$$f_{tr} = \text{Sup}\left[1 - 100\left(\frac{f_v^{(Ti,Nb)C}(t)}{f_{v,eq}^{(Ti,Nb)C}(t)} - 1\right)^2 ; 0\right] \tag{26}$$

which ensures that if $f_v^{(Ti,Nb)C}(t) << f_{v,eq}^{(Ti,Nb)C}(t)$ then $f_{tr} \approx 0$ and coarsening cannot begin, while if $f_{v,eq}^{(Ti,Nb)C}$ is reached then $f_{tr} \approx 1$. The growth of precipitates cannot happen anymore by pumping solute from the surrounding matrix.

Diffusivities of Ti/Nb are assumed to be affected by dislocation density and their values fitted in ferrite, bainite and martensite. A very wide variety of solubility product values can be found in DeArdo and Gladman works[63,64] for TiC and NbC in ferrite. The values used in our model are also fitted.

2. *Interactions between transformations*
Literature has shown that austenite formation kinetics are deeply dependent on the recrystallized fraction when Ac1 temperature is reached. For this reason, the interaction between these two transformations has been a topic of interest for a long time.[6,7,10,12–14,16,19,23,24] Consensus is that austenite formation kinetics are accelerated when austenite forms in non-recrystallized areas of the microstructure. This effect is thought to be

Table IV. Parameters Used for the Microalloying Elements Precipitation Model

Parameter		Value	Units	Literature Values
$N^0_{(Ti,Nb)C}$	Nucleation sites density for (Ti,Nb)C $(2/a^3_{bcc})$	$8.55 \cdot 10^{28}$	m^{-3}	—
$D^{\alpha_{REX}}_{Ti,Nb}$	Prefactor for Ti/Nb diffusion in recrystallized ferrite (fit)	1×10^{-4}	m^2 s^{-1}	1.27×10^{-5} to 7×10^{-3}[24,62,63]
$D^{\alpha_B}_{Ti,Nb}$	Prefactor for Ti/Nb diffusion in bainite (fit)	1×10^{-3}.	m^2 s^{-1}	
$D^{\alpha'}_{Ti,Nb}$	Prefactor for Ti/Nb diffusion in martensite (fit)	3×10^{-2}	m^2 s^{-1}	
$Q_{Ti,Nb}$.	Activation energy for Ti/Nb diffusion	250,000.	J mol^{-1}.	224,000 to 252,000[24,58,62]
$\gamma_{(Ti,Nb)C}$.	Interfacial energy of (Ti,Nb)C in ferrite	0.72	J m^{-2}	0.49 to 0.78[33,58]
$A; B$	Solubility product parameters for (Ti,Nb)C in ferrite (fit)	10500; 4	K; —	[63,64]
V^P_m	(Ti,Nb)C molar volume	12.96×10^{-6}	m^3 mol^{-1}	—
V^P_{at}	(Ti,Nb)C atomic volume	1.11×10^{-29}.	m^{-3}	—
$X^{eq}_C(T)$	Solubility limit of C in recrystallized ferrite	$0.01 \exp(-28400/RT)$.	—	[34]

due to a larger nucleation site density. To model this interaction, we use the following correction to express the *effective* nucleation site density for austenite:

$$N\gamma = \frac{N^0_\gamma}{f_{REX}(Ae1)^2} \qquad [27]$$

Invertedly, several authors observed a stagnation of recrystallization kinetics once austenite had appeared in the microstructure.[16,19,20,23] Such an effect is seen in this work at 10 °C/s (see Figure 6(d)). This interaction might be due to austenite nucleation consuming the remaining nucleation sites for recrystallization, but also to competing migration of recrystallization and austenitization interfaces. Moreover, as austenite nucleation is favored in non-recrystallized zones, these zones are more likely to be transformed into austenite than recrystallized ones, thus resulting in inhibition of recrystallization. $f^{crit}_\gamma = 10$ pct was found to be a good critical value for the austenite fraction above which recrystallization would be stopped. Ollat et al.[23] used the same value. The interaction is easily transcribed by the following condition:

$$\text{if}\left(df_{REX} > 0 \quad \text{and} \quad f_\gamma > f^{crit}_\gamma\right) \quad \text{then} \quad df_{REX} = 0 \quad [28]$$

Microalloying elements are expected to hinder recrystallization kinetics by the combination of a solute drag effect and Zener-pinning of $\alpha_{REX}/\alpha_{NREX}$ grain boundaries. Following Sinclair et al.,[31] effective mobility of recrystallized grain boundaries is:

$$M_{REX}(t) = \frac{M^0_{REX}(t)}{1 + \alpha_{Ti,Nb} x^{ss}_{Ti,Nb}(t) M^0_{REX}(t)} \qquad [29]$$

in which $x^{ss}_{Ti,Nb}(t)$ is the fraction of microalloying elements in solid solution and $\alpha_{Ti,Nb}$ their solute drag coefficient (dimensionless). A value of 4.1×10^3 was used for $\alpha_{Ti,Nb}$, following the work of Bellavoine et al.[24] and the initially available quantities of Ti and Nb in solid solution in the studied steel. Net recrystallization driving force is:

$$G_{REX}(t) = G^0_{REX}(t) - \frac{3}{2}\gamma_{GB}\frac{f^{(Ti,Nb)C}_v(t)}{R_{(Ti,Nb)C}(t)} \qquad [30]$$

Microalloying elements diffusivities are increased in non-recrystallized parts of the microstructure, as lattice defects act as high-diffusivity paths. Therefore, recrystallization progression reduces the effective diffusivity of microalloying elements. A mixture law is used to consider this:

$$D^{eff}_{Ti,Nb}(T) = \tau_{REX} D^{\alpha_{REX}}_{Ti,Nb}(T) + (1 - \tau_{REX})D^{\alpha_B,\alpha'}_{Ti,Nb}(T) \quad [31]$$

with $\tau_{REX} = f_{REX}/(f_{REX} + f_{NREX})$ being the recrystallization ratio.

Finally, how microalloying elements precipitation kinetics might interact with austenite formation has not been found in existing literature. Girina et al.[32]

indicate an acceleration of austenite formation kinetics in Nb-containing steels, compared to Nb-free ones, but this could be the result of incomplete recrystallization. Gouné et al.[59] calculate that the driving force for austenite formation, of around 15,000 kJ m^{-3}, is much higher than the Zener-pinning force of microalloying elements (1875 kJ m^{-3}) for their steel (0.163 wt pct Ti). Therefore, it can be safely assumed that (Ti,Nb)C precipitation does not directly interfere with austenite formation in this work. No interaction is implemented in the model.

3. Modelling results

The main results obtained with our model for slow heating (1 °C/s) are presented in Figure 4. Calculated recrystallization kinetics (Figure 4(a)) are in agreement with experimental values, and so are austenite formation kinetics. However, recrystallization kinetics in martensite and bainite do not correspond to what has been experimentally observed (Figure 4(b)). Indeed, recrystallization is completed in bainite before martensite, and parts of martensite do not recrystallize before austenite formation. The results obtained with the model do not transcribe this phenomenon. No parameters ensemble that would allow to keep a good global agreement (recrystallization + austenite formation + (Ti,Nb)C precipitation kinetics) and relate delayed recrystallization in martensite has been found. It is thus concluded that recrystallization mechanisms in bainite and martensite are not well accounted for in the model.

Concerning microalloying elements precipitation (Figure 4(c)), the calculated kinetics reproduces well experimental data.

C. Interaction Between Cementite Precipitation and Recrystallization

The study of microstructural changes left aside an important interaction regarding recrystallization. A comparison of recrystallized and non-recrystallized zones (Figure 5(a)) during slow heating (up to 670 °C) shows that recrystallized zones are located where carbides are few and coarsened, whereas non-recrystallized zones coincide with numerous, small carbides. This indicates that carbides growth and coarsening interact with recrystallization.

Further insight is given by a TEM observation of the recrystallization process (Figure 5(b)). On the center of the micrograph lies a non-recrystallized zone (in dark), surrounded by recrystallized grains. Carbides are dispersed in recrystallized grains but also on $\alpha_{REX}/\alpha_{REX}$ grain boundaries. Most importantly, $\alpha_{REX}/\alpha_{NREX}$ boundaries are pinned by cementite particles (green-dashed circles). Recrystallized grain boundaries movement is therefore hindered by cementite presence. This effect of cementite had already been noticed in several studies[12,19] during pearlite spheroidization, but had not been discussed any further. Hence, recrystallization kinetics could be limited in cementite-rich zones of the microstructure, i.e. martensite.

D. Modelling with Cementite Precipitation

1. Model particularities

Cementite precipitation kinetics are also calculated with Deschamps-Bréchet model. Used parameters are given in Table V. It is approximated that cementite precipitation only occurs in martensite, where most of carbon lies in solid solution. The precipitation of transition carbides is neglected, and cementite dissolution during austenite formation is not modelled. Cementite volume fraction is also neglected when calculating phase fractions ($f_{REX} + f_{NREX} + f_\gamma = 1$).

Deschamps–Bréchet model is based on homogeneous nucleation. This hypothesis is not valid for cementite, as it is known that it preferentially nucleates on dislocations, laths boundaries, prior austenite grain boundaries, etc.[35,65] The chosen value for cementite interfacial energy is, therefore, an effective value (0.268 J m^{-2}), much lower than the one of 0.74 J m^{-2} already reported in the literature.[35,66] It is however closer to the values reported in similar models by Perez and Deschamps (0.174 J m^{-2}) and Yang et al. (0.151 J m^{-2}).[34,36]

Then, every atom along a dislocation core is a potential cementite nucleation site.[35,67] N_θ is set equal to $\rho_0^{\alpha'}/a$, where a is the mean atomic distance (2×10^{-10} m in ferrite), giving a value of 6.6×10^{24} m^{-3}. Finally, carbon diffusivity in martensite is considered lower than that in ferrite due to lattice distortion, as originally proposed by Hillert.[68] Recent measurements of $D_C^{\alpha'}$ by Maugis et al.[69] confirm this.

Assuming that (Ti,Nb)C and cementite nucleate independently,[34] the two precipitation models are coupled through the carbon mass balance:

$$x_C^{ss}(t) = x_C^{ss,0} - f_v^\theta(t) \frac{V_m^\alpha}{V_m^\theta} - f_v^{(Ti,Nb)C}(t) \frac{V_m^\alpha}{V_m^P} \quad [32]$$

$$f_{v,eq}^\theta(t) = \left(x_C^{ss,0} - f_v^{(Ti,Nb)C}(t) \frac{V_m^\alpha}{V_m^P} - x_c^{ss,eq} \right) \frac{V_m^\theta}{V_m^\alpha} \quad [33]$$

The effect of cementite on recrystallization is considered through Zener-pinning of grain boundaries. Simplest assumption is that the pinning forces exerted by (Ti,Nb)C and cementite can be considered additive. The net recrystallization driving force in martensite now writes:

$$G_{REX}^{\alpha'}(t) = G_{REX}^0(t) - \frac{3}{2} \gamma_{GB} \left(\frac{f_v^{(Ti,Nb)C}(t)}{R_{(Ti,Nb)C}(t)} + \frac{f_v^\theta(t)}{R_\theta(t)} \right) \quad [34]$$

Dislocation density value in martensite was adjusted from $\rho_0^{\alpha'} = 1 \times 10^{15}$ m^{-2} to $\rho_0^{\alpha'} = 2 \times 10^{15}$ m^{-2} so that the best fit could be obtained between calculated kinetics and experimental ones now that cementite precipitation is considered. All other parameters are left unchanged.

2. Results

The results obtained with our model are given in Figures 6(a) through (h). Excellent agreement is
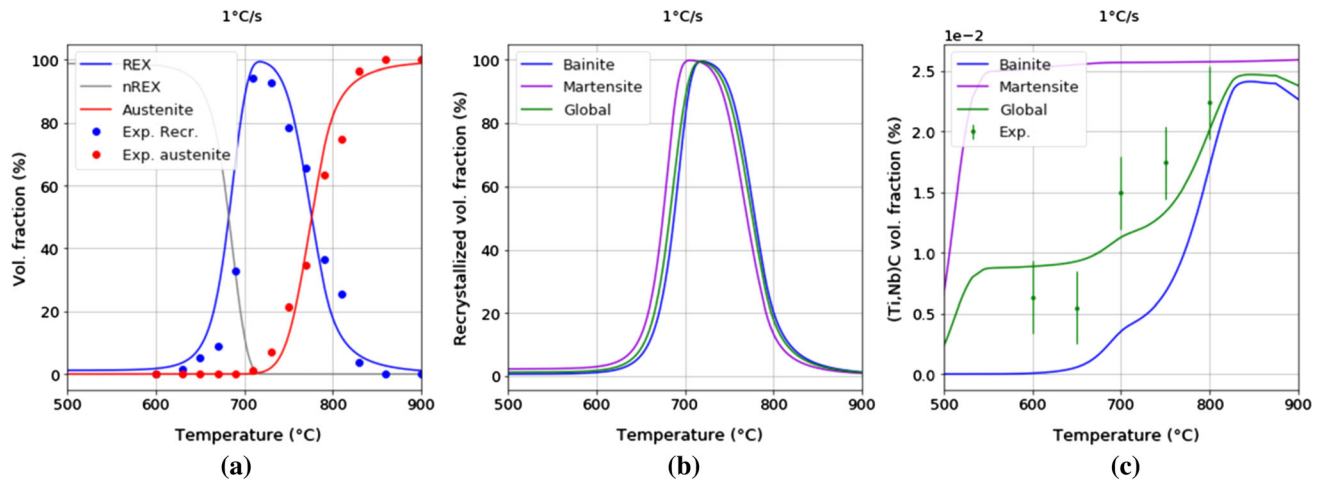
Fig. 4—1 °C/s heating rate: (*a*) Recrystallization and austenite formation kinetics; (*b*) Recrystallization kinetics in bainite and martensite; (*c*) Microalloying elements precipitation kinetics.
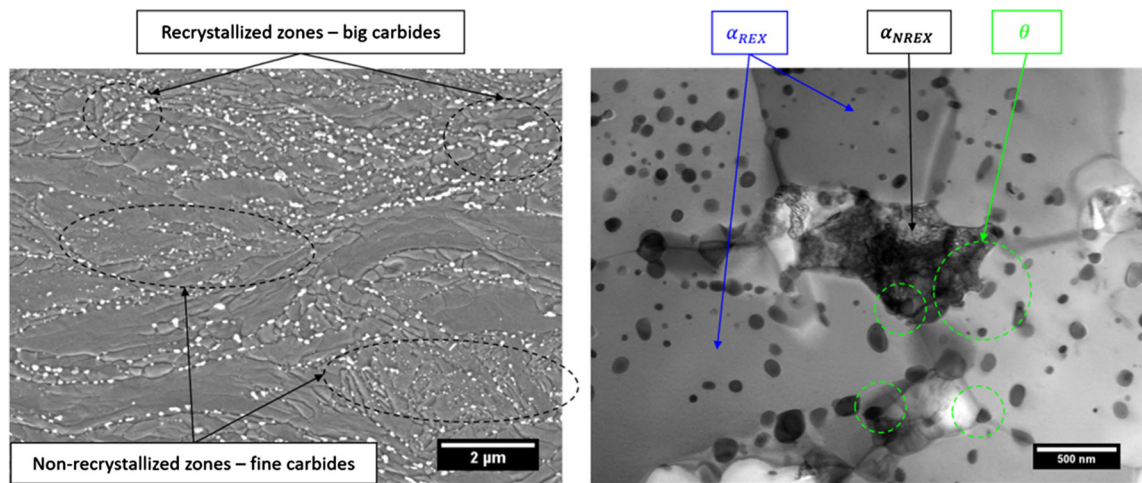

Fig. 5—(*a*) FEG-SEM observation (1 °C/s to 670 °C) of big and fine, dispersed carbides in recrystallized and non-recrystallized zones, respectively; (*b*) TEM observation (1 °C/s to 700 °C) of cementite particles pinning $\alpha_{REX}/\alpha_{REX}$ and $\alpha_{REX}/\alpha_{NREX}$ grain boundaries.

Table V. Parameters Used for the Cementite Precipitation Model

	Parameter	Value	Units	Literature Values
N_θ^0	Nucleation sites density for cementite	6.6×10^{24}	m^{-3}	—
D_C^α	Prefactor for C diffusion in recrystallized ferrite	2×10^{-6}	$m^2\,s^{-1}$	[70]
$D_C^{\alpha'}$	Prefactor for C diffusion in martensite	1×10^{-7}	$m^2\,s^{-1}$	$2 \times 10^{-6[35]}$
Q_C^α	Activation energy for C diffusion in recrystallized ferrite	84,100	$J\,mol^{-1}$	[70]
$Q_C^{\alpha'}$	Activation energy for C diffusion in martensite	108,000	$J\,mol^{-1}$	[35]
γ_θ	Interfacial energy of cementite in ferrite	0.268	$J\,mol^{-2}$	0.151 to 0.174 [36,34]
V_m^θ	Molar volume of cementite	23.3×10^{-6}	$m^3\,mol^{-1}$	—

obtained between global recrystallization kinetics, austenite formation kinetics and experimental data for slow heating simulation (1 °C/s – (a)). Moreover, individual recrystallization kinetics (Figure 6(b)) are now consistent with metallographic observations: recrystallization is not complete in martensite, whereas bainite is fully recrystallized when T = Ac1 = 710 °C is reached. The faster decrease of f_{REX} in martensite than in bainite indicates faster austenite formation in this phase. This result is compatible with the genesis of a banded microstructure. Microalloying elements precipitation kinetics are also in good agreement with

experimental data (Figure 6(c)). Cementite volume fraction evolution at 1 °C/s is presented in Figure 6(g), along with its mean radius in Figure 6(h). The calculated volume fraction is in accordance with experimental measurements. Equilibrium fraction is reached at around $T = 450$ °C, suggesting the end of martensite tempering. Calculated mean radius is also close to the one determined experimentally.

Fast heating is also simulated. Global recrystallization and austenite formation kinetics are presented in Figure 6(d). Once again, good agreement with experiment is found. The recrystallization stagnation phenomenon is well-reproduced. No recrystallization is calculated in martensite (Figure 6(e)), which fits our observations. Bainite only partly recrystallizes before the beginning of austenite formation. Microalloying elements precipitation kinetics are also in agreement with experimental data (Figure 6(f)). Cementite volume fraction (Figure 6(g), dotted line) at 700 °C is consistent with experience but is too high for lower temperatures. This discrepancy could be attributed to the absence of C in bainite in our model. Finally, cementite mean radius is close to the experimentally determined one (Figure 6(h), dotted line).

Considering cementite precipitation in the model leads to excellent agreement between calculated kinetics and experimental ones at both heating rates. Cementite showed to have a strong delaying effect on recrystallization, leading to incomplete recrystallization in martensite before austenite formation. The interaction between recrystallization and austenite formation, modelled through the evolution of nuclei density for austenite, then allows for good reproduction of austenitization kinetics. It is concluded that cementite presence in steels should not be carelessly neglected, as it can have dramatic effects on the kinetics of subsequent transformations.

IV. EFFECTS OF CEMENTITE AND MICROALLOYING ELEMENTS ON RECRYSTALLIZATION KINETICS

A. Recrystallization Driving Force

The effect of cementite on recrystallization of martensite has been considered by Zener-pinning, resulting in a diminution of the net recrystallization driving force in martensite $G_{REX}^{\alpha'}$. The evolution of $G_{REX}^{\alpha'}$, either considering or neglecting cementite and (Ti,Nb)C pinning effects, is drawn with corresponding recrystallization kinetics in Figures 7(a) and (b) for slow heating, and in Figures 7(c) and (d) for fast heating. Evolution of $G_{REX}^{\alpha'}$ is plotted up to $T = Ac1$ only, since austenite growth prevents recrystallization from happening above this temperature.

During slow heating (Figure 7(a)), $G_{REX}^{\alpha'}$ does not differ much from the pure driving force for recrystallization if one only considers the microalloying elements pinning effect (+ (Ti,Nb)C case). The recrystallization kinetics are indeed only slightly delayed to higher temperatures (Figure 7(b)). Considering cementite

pinning (+ θ case) however leads to a strong reduction of $G_{REX}^{\alpha'}$. $G_{REX}^{\alpha'}$ then increases again from around $T = 550$ °C along with cementite coarsening, which reduces f_v^{θ}/R_{θ} ratio and lowers its pinning effect. A delay of recrystallization kinetics is thus observed in martensite. Only with cementite pinning is recrystallization significantly delayed in martensite. Its recrystallization kinetics indeed become very close to those of bainite. Considering cementite *and* microalloying elements pinning (+ θ + (Ti,Nb)C case) finally leads to enough delay in martensite recrystallization kinetics to make it incomplete at $T = Ac1 = 710$ °C. It is the only scenario in which bainite is the most-recrystallizing phase of the microstructure. Cementite thus proves to have a stronger pinning effect than (Ti,Nb)C particles during slow heating, which makes it responsible for the recrystallization kinetics in martensite, and therefore of the banded microstructure that forms.

Results are similar for fast heating. Only considering microalloying elements pinning effect does not induce a very strong variation of $G_{REX}^{\alpha'}$, thus giving close recrystallization kinetics for the pure and + (Ti,Nb)C cases (Figures 7(c) and (d)). However, cementite consideration once again strongly reduces $G_{REX}^{\alpha'}$ around $T = 400$ °C. Fast-heating leads to the precipitation of finer particles, giving a higher value to f_v^{θ}/R_{θ} ratio than in the slow-heating case, and therefore, giving cementite an even stronger delaying effect on recrystallization kinetics. Coarsening of particles is also limited in the considered temperature range. Martensite cannot recrystallize anymore.

Therefore, it is concluded that cementite presence is the most important parameter to acknowledge regarding the recrystallization kinetics of our steel. Consequently, carbon nominal content of the steel is a crucial parameter whose effect on recrystallization kinetics should be investigated.

B. Influence of Carbon Nominal Content on Recrystallization Kinetics

The recrystallization kinetics of martensite are calculated for different levels of carbon nominal content (w_C^0 =0.075, 0.1, 0.15 and 0.2 wt pct) for both heating rates, as equilibrium volume fraction of cementite directly depends on w_C^0. These nominal contents correspond to martensite C enrichments $w_C^{\alpha'}$ of 0.185, 0.26, 0.41 and 0.54 wt pct respectively, other things being equal. The evolution of the recrystallization driving force of martensite $G_{REX}^{\alpha'}$ and corresponding recrystallization kinetics are drawn for 1 °C/s heating in Figures 8(a) and (b), and for 10 °C/s heating in Figures 8(c) and (d). (Ti,Nb)C pinning effect is considered in all cases.

During slow heating (Figures 8(a) and (b)), the recrystallization driving force $G_{REX}^{\alpha'}$ is not significantly altered by carbon content if $w_C^{\alpha'} \leq 0.26$ wt pct. The $G_{REX}^{\alpha'}$ decrease magnitude is indeed comparable to the +(Ti,Nb)C case previously shown (Figure 7(a)). Recrystallization kinetics are only delayed to higher
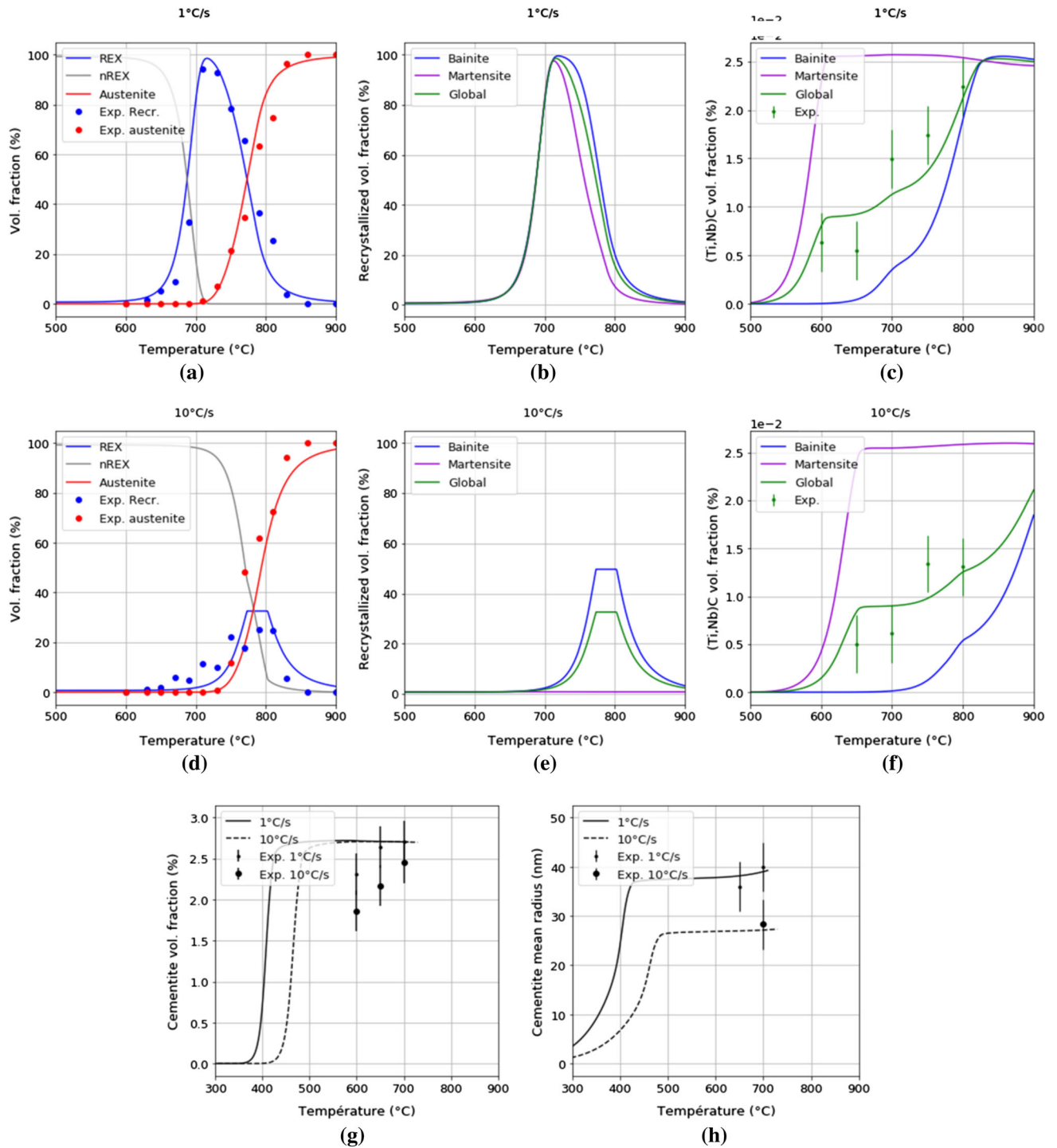
Fig. 6—(a) 1 °C/s—Recrystallization and austenite formation kinetics; (b) 1 °C/s—Recrystallization kinetics in bainite and martensite; (c) 1 °C/s—Microalloying elements precipitation kinetics; (d) 10 °C/s—Recrystallization and austenite formation kinetics; (e) 10 °C/s—Recrystallization kinetics in bainite and martensite; (f) 10 °C/s—Microalloying elements precipitation kinetics; (g) Cementite precipitation kinetics for 1 and 10°C/s heating rates (plotted up to $T = $ Ac1 only); (h) Cementite mean radius for 1 and 10 °C/s heating rates (plotted up to $T = $ Ac1 only).

temperatures for $w_C^0 \geq 0.41$ wt pct. (Figure 8(b)). It is, however, only with $w_C^{\alpha'} = 0.54$ wt pct C that recrystallization becomes incomplete in martensite when $T = $ Ac1 is reached, leading to the formation of a banded microstructure. Consequently, low carbon enrichments of martensite are to be preferred to ensure full

recrystallization of bainite-martensite initial microstructures before austenite formation, if slow heating is applied. This is consistent with previous literature results.[18,24]

During fast heating, $G_{REX}^{\alpha'}$ becomes more sensitive to $w_C^{\alpha'}$ due to finer cementite particles being precipitated
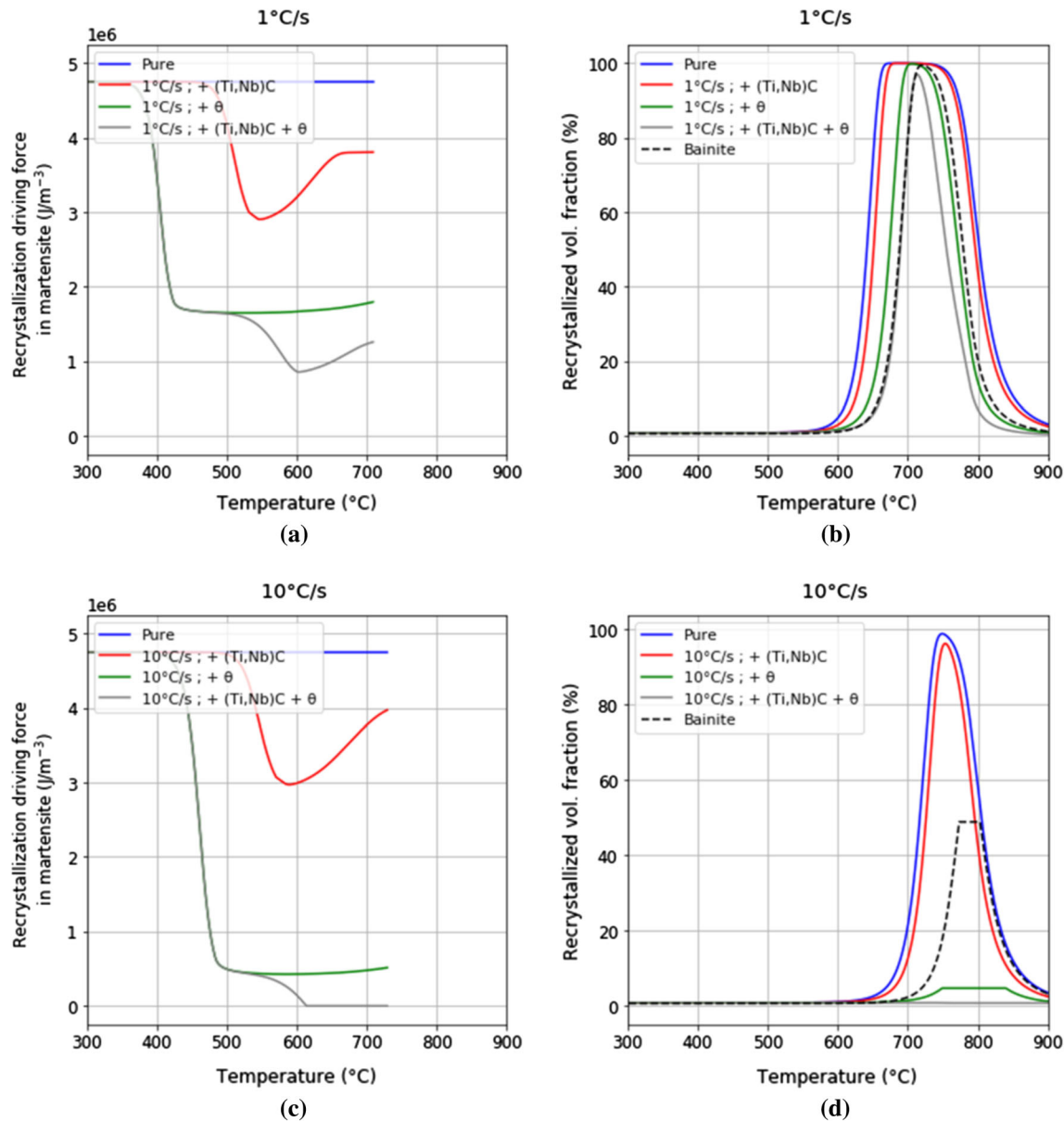
Fig. 7—(a) 1 °C/s—Recrystallization driving force in martensite with or without considering microalloying elements and cementite precipitation (plotted up to T = Ac1 only); (b) 1 °C/s—Corresponding recrystallization kinetics of martensite compared to those in bainite; (c) 10 °C/s—Recrystallization driving force in martensite with or without considering microalloying elements and cementite precipitation (plotted up to T = Ac1 only); (d) 10 °C/s—Corresponding recrystallization kinetics of martensite compared to those in bainite.

(Figure 8(c)). Recrystallization of martensite is very close to recrystallization of bainite for $w_C^{\alpha'}$ =0.41 wt pct. Above 0.41 wt pct, recrystallization is fully inhibited in martensite.

Those calculations show that carbon content of martensite is an important parameter to consider when tuning a steel chemistry. For a bainite-martensite initial microstructure such as the one studied (65 vol pct bainite, 35 vol pct martensite), w_C^0 should not be chosen above 0.15 wt pct, as enough cementite would precipitate to prevent the steel from fully recrystallizing, even for low heating rates. It is thus very likely to obtain banded microstructures if the carbon nominal content is not set low enough.

V. SUMMARY

This work took interest in the microstructural changes underwent by a cold-rolled, Ti-Nb microalloyed high-formability steel with a bainite–martensite initial microstructure during 1 and 10 °C/s heating. It has been shown that banded microstructures were obtained for both heating rates due to incomplete (1 °C/s) and absence of recrystallization (10 °C/s) of martensite.

Experimental data suggested that the incomplete recrystallization phenomenon in martensite could be attributed to cementite. TEM observation indeed showed that $\alpha_{REX}/\alpha_{NREX}$ grain boundaries are pinned by cementite particles. A model based on JMAK theory (austenite formation and recrystallization) and classical
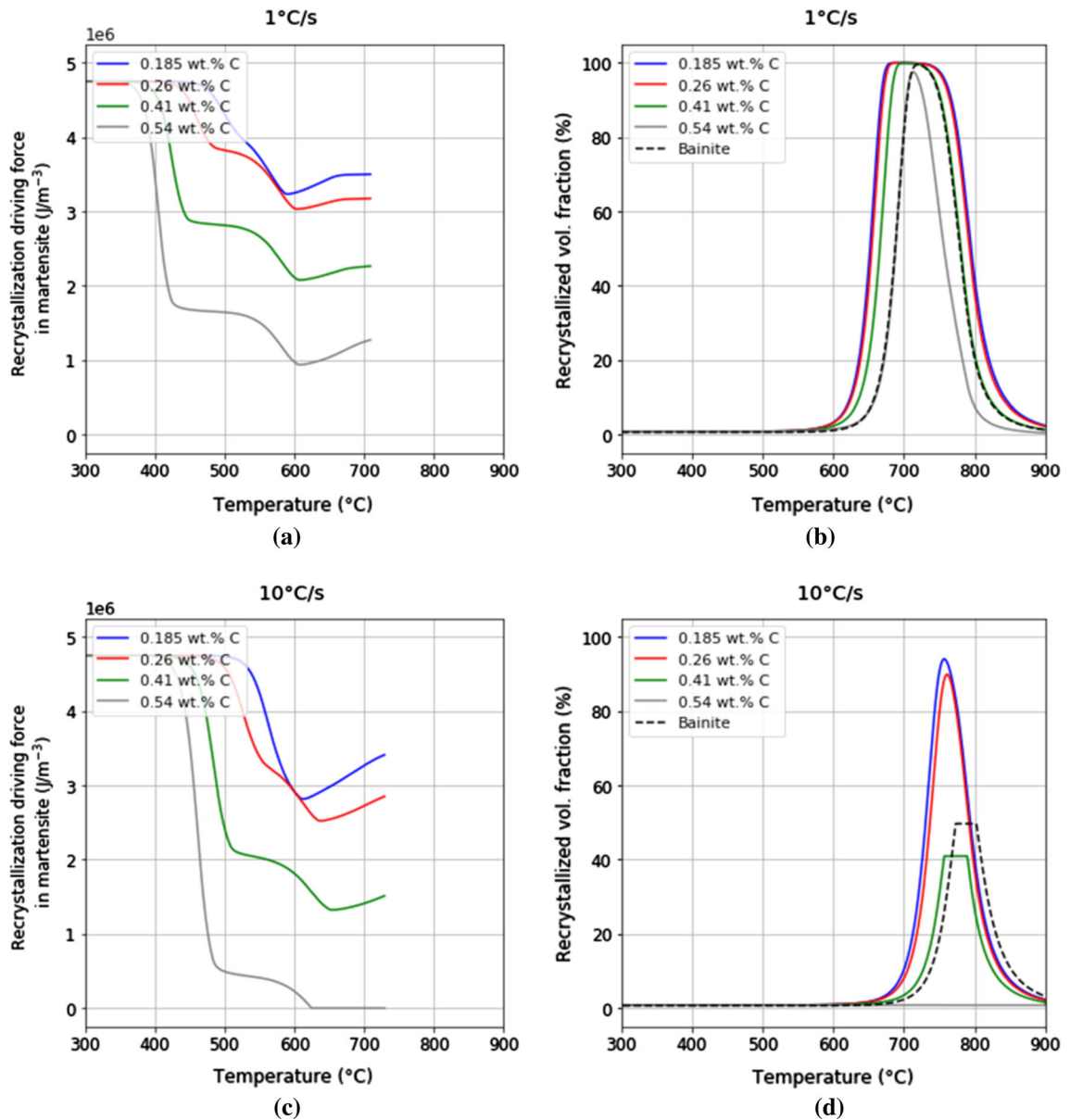
Fig. 8—(*a*) 1 °C/s—Recrystallization driving force in martensite for different carbon contents (plotted up to $T = Ac1$ only); (*b*) 1 °C/-s—Corresponding martensite recrystallization kinetics compared to those of bainite; (*c*) 10 °C/s—Recrystallization driving force in martensite for different carbon contents (plotted up to $T = Ac1$ only); (*d*) 10 °C/s—Corresponding martensite recrystallization kinetics compared to those of bainite.

nucleation theory for nucleation, growth and coarsening of (Ti,Nb)C precipitation and cementite precipitation was developed to simulate microstructural changes.

Calculations confirmed that the delayed martensite recrystallization kinetics during slow heating were a consequence of cementite precipitation in this phase. Fast-heating calculations also reproduced the total inhibition of recrystallization in martensite.

These results show that cementite precipitation is of prime importance, since its effect on the recrystallization driving force is much more important than microalloying elements precipitation. Consequently, carbon enrichment of martensite, and therefore, carbon nominal content of the steel were shown to be of utmost importance regarding the recrystallization kinetics. Low-carbon steels (0.1 wt pct C and less) should be preferred to ensure full recrystallization before austenite formation and prevent the formation of banded microstructures, which are detrimental to good in-use properties.

and assistance. Dr. G. Da Rosa is also gratefully acknowledged for fruitful discussions about microstructural evolutions.

REFERENCES

1. O. Bouaziz, H. Zurob, and M. Huang: *Steel Res. Int.*, 2013, vol. 12, pp. 937–47.
2. D. Bhattacharya: *Tecnol. Metal. Mater. Miner.*, 2014, vol. 11, pp. 371–83.
3. N. Fonstein: *Advanced High Strength Sheet Steels: Physical Metallurgy, Design, Processing, and Properties*, Springer, Berlin, 2015.
4. C.I. Garcia and A.J. Deardo: *Metall. Trans. A*, 1981, vol. 12, pp. 521–30.
5. G.R. Speich, V.A. Demarest, and R.L. Miller: *Metall. Mater. Trans. A*, 1981, vol. 12, pp. 1419–28.
6. D.Z. Yang, E.L. Brown, D.K. Matlock, and G. Krauss: *Metall. Trans. A*, 1985, vol. 16, pp. 1385–92.
7. J. Huang, W.J. Poole, and M. Militzer: *Metall. Mater. Trans. A*, 2004, vol. 35, pp. 3363–75.
8. F.G. Caballero, A. García-Junceda, C. Capdevila, and C. García de Andrés: *Mater. Trans.*, 2006, vol. 47, pp. 2269–76.
9. D. San Martín, T. de Cock, A. García-Junceda, F.G. Caballero, C. Capdevila, and C.G. de Andrés: *Mater. Sci. Technol.*, 2008, vol. 24, pp. 266–72.
10. T. Ogawa, N. Maruyama, N. Sugiura, and N. Yoshinaga: *ISIJ International*, 2010, vol. 50, pp. 46–475.
11. V.H. Baltazar Hernandez, S.S. Nayak, and Y. Zhou: *Metall. Mater. Trans. A*, 2011, vol. 42, pp. 3115–29.
12. H. Azizi-Alizamini, M. Militzer, and W.J. Poole: *Metall. Mater. Trans. A*, 2011, vol. 42, pp. 1544–57.
13. M. Kulakov, W.J. Poole, and M. Militzer: *Metall. Mater. Trans. A*, 2013, vol. 44, pp. 3564–76.
14. P. Li, J. Li, Q. Meng, W. Hu, and D. Xu: *J. Alloys Compd.*, 2013, vol. 578, pp. 320–27.
15. R. Wei, M. Enomoto, R. Hadian, H.S. Zurob, and G.R. Purdy: *Acta Mater.*, 2013, vol. 61, pp. 697–707.
16. A. Chbihi, D. Barbier, L. Germain, A. Hazotte, and M. Gouné: *J. Mater. Sci.*, 2014, vol. 49, pp. 3608–21.
17. M. Kulakov, W.J. Poole, and M. Militzer: *ISIJ Int.*, 2014, vol. 54, pp. 2627–36.
18. C. Philippot, J. Drillet, P. Maugis, V. Hebert, and M. Dumont: *Metall. Res. Technol.*, 2014, vol. 111, pp. 3–8.
19. D. Barbier, L. Germain, A. Hazotte, M. Gouné, and A. Chbihi: *J. Mater. Sci.*, 2015, vol. 50, pp. 374–81.
20. T. Ogawa: *Int. J. Mech. Mater. Eng.*, 2015, vol. 10, p. 22.
21. F. CastroCerda, B. Schulz, S. Papaefthymiou, A. Artigas, A. Monsalve, and R. Petrov: *Metals*, 2016, vol. 6, p. 321.
22. F.M. CastroCerda, I. Sabirov, C. Goulas, J. Sietsma, A. Monsalve, and R.H. Petrov: *Mater. Des.*, 2017, vol. 116, pp. 448–60.
23. M. Ollat, V. Massardier, D. Fabregue, E. Buscarlet, F. Keovilay, and M. Perez: *Metall. Mater. Trans. A*, 2017, vol. 48, pp. 4486–99.
24. M. Bellavoine, M. Dumont, J. Drillet, V. Hébert, and P. Maugis: *Metall. Mater. Trans. A*, 2018, vol. 49, pp. 2865–75.
25. J.J. Jonas and I. Weiss: *Metal. Sci.*, 1979, vol. 13, pp. 238–45.
26. A. Deschamps, F. Livet, and Y. Bréchet: *Acta Mater.*, 1998, vol. 47, pp. 281–92.
27. A. Deschamps and Y. Bréchet: *Acta Mater.*, 1998, vol. 47, pp. 293–305.
28. H.S. Zurob, Y. Brechet, and G. Purdy: *Acta Mater.*, 2001, vol. 49, pp. 4183–90.
29. V. Andrade-Carozzo and P. Jacques: *Mater. Sci. Forum*, 2007, vols. 539–543, pp. 4649–54.
30. Y.J.M. Bréchet, C.R. Hutchinson, H.S. Zurob, and C.W. Sinclair: *Steel Res. Int.*, 2007, vol. 78, pp. 210–15.
31. C.W. Sinclair, C.R. Hutchinson, and Y. Bréchet: *Metall. Mater. Trans. A*, 2007, vol. 38, pp. 821–30.
32. O. Girina, N. Fonstein, and D. Bhattacharya: vol. 1 : Plenary Lectures Automotive Applications, Oils and Gas Applications, High Temperature Applications of High Strength Steels, Buenos Aires, 2008, pp. 29–35.
33. C.R. Hutchinson, H.S. Zurob, C.W. Sinclair, and Y.J.M. Brechet: *Scr. Mater.*, 2008, vol. 59, pp. 635–37.
34. M. Perez and A. Deschamps: *Mater. Sci. Eng. A*, 2003, vol. 360, pp. 214–19.
35. Y. Wang, S. Denis, B. Appolaire, and P. Archambault: *J. Phys. IV France*, 2004, vol. 120, pp. 103–10.
36. Y. Yang, B. Wang, Z.D. Wang, Y.M. Li, G.D. Wang, and R.D.K. Misra: in *Materials Science Forum*, vol. 898, Trans Tech Publ, 2017, pp. 832–39.
37. J. Schindelin, I. Arganda-Carreras, E. Frise, V. Kaynig, M. Longair, T. Pietzsch, S. Preibisch, C. Rueden, S. Saalfeld, B. Schmid, J.-Y. Tinevez, D.J. White, V. Hartenstein, K. Eliceiri, P. Tomancak, and A. Cardona: *Nature Methods*, 2012, vol. 9, p. 676.
38. F.J. Humphreys and M. Hatherly: *Recrystallization and Related Annealing Phenomena*, 2nd ed., Elsevier, New York, 2004.
39. W. Johnson and R. Mehl: *Trans. AIME.*, 1939, vol. 135, pp. 416–58.
40. M. Avrami: *J. Chem. Phys.*, 1939, vol. 7, pp. 1103–12.
41. M. Avrami: *J. Chem. Phys.*, 1940, vol. 8, pp. 212–24.
42. M. Avrami: *J. Chem. Phys.*, 1941, vol. 9, pp. 177–84.
43. A.N. Shiryayev: in *Selected Works of A. N. Kolmogorov*, A.N. Shiryayev, ed., Springer Netherlands, Dordrecht, 1992, pp. 188–92.
44. J.-O. Andersson, T. Helander, L. Höglund, P. Shi, and B. Sundman: *Calphad*, 2002, vol. 26, pp. 273–12.
45. *Thermo-Calc Software TCFE9 Steels/Fe-Alloys Database* (Accessed on 26.09.2019).
46. C. Bos, M.G. Mecozzi, and J. Sietsma: *Comput. Mater. Sci.*, 2010, vol. 48, pp. 692–9.
47. E. Gamsjäger, H. Chen, and S. van der Zwaag: *Comput. Mater. Sci.*, 2014, vol. 83, pp. 92–100.
48. M.G. Mecozzi, C. Bos, and J. Sietsma: *Acta Mater.*, 2015, vol. 88, pp. 302–13.
49. C. Zheng and D. Raabe: *Acta Mater.*, 2013, vol. 61, pp. 5504–17.
50. M. Hillert and L. Höglund: *Scr. Mater.*, 2006, vol. 54, pp. 1259–63.
51. F. Huyan, J.-Y. Yan, L. Höglund, J. Ågren, and A. Borgenstam: *Metall. Mater. Trans. A*, 2018, vol. 49, pp. 1053–60.
52. E. Gamsjäger, M. Militzer, F. Fazeli, J. Svoboda, and F.D. Fischer: *Comput. Mater. Sci.*, 2006, vol. 37, pp. 94–100.
53. Y.X. Wu, W.W. Sun, M.J. Styles, A. Arlazarov, and C.R. Hutchinson: *Acta Mater.*, 2018, vol. 159, pp. 209–24.
54. B. Zhu and M. Militzer: *Modelling Simul. Mater. Sci. Eng.*, 2012, vol. 20, art. no. 085011.
55. M. Gouné, P. Maugis, and F. Danoix: *Nanotechnol. Rev.*, 2015, vol. 4, pp. 517–32.
56. P. Maugis and M. Gouné: *Acta Materialia*, 2005, vol. 53, pp. 3359–67.
57. B. Noble and S.E. Bray: *Mater. Sci. Eng. A*, 1999, vol. 266, pp. 80–85.
58. M. Perez, E. Courtois, D. Acevedo, T. Epicier, and P. Maugis: *Philos. Mag. Lett.*, 2007, vol. 87, pp. 645–56.
59. M. Gouné, J. Drillet, and P. Maugis: *Computat. Mater. Sci.*, 2012, vol. 55, pp. 127–35.
60. J.H. Jang, C.-H. Lee, H.N. Han, H.K.D.H. Bhadeshia, and D.-W. Suh: *Mater. Sci. Technol.*, 2013, vol. 29, pp. 1074–79.
61. D. Gendt: Thèse de doctorat, Université Paris XI, 2001.
62. F. Perrard, A. Deschamps, and P. Maugis: *Acta Mater.*, 2007, vol. 55, pp. 1255–66.
63. T. Gladman: *The Physical Metallurgy of Microalloyed Steels*, Maney, London, 2002.
64. A.J. DeArdo: *Int. Mater. Rev.*, 2003, vol. 48, pp. 371–402.
65. L.E. Samuels: *Metallogr. Microstruct. Anal.*, 2014, vol. 3, pp. 70–90.
66. J.W. Martin, R.D. Doherty, and B. Cantor: *Stability of Microstructure in Metallic Systems*, 2nd ed., Cambridge University Press, Cambridge, 1997.
67. S. Zamberger, L. Whitmore, S. Krisam, T. Wojcik, and E. Kozeschnik: *Modelling Simul. Mater. Sci. Eng.*, 2015, vol. 23, p. 055012.
68. M. Hillert: *Acta Metall.*, 1959, vol. 7, pp. 653–58.
69. P. Maugis, F. Danoix, M. Dumont, S. Curelea, S. Cazottes, H. Zapolsky, and M. Gouné: *Mater. Lett.*, 2018, vol. 214, pp. 213–16.

70. D.A. Porter and K.E. Easterling: *Phase Transformations in Metals and Alloys*, 3rd ed., Springer, New York, 1992.